PERGAMON

International Journal of Heat and Mass Transfer 45 (2002) 4857–4869

International Journal of HEAT and MASS TRANSFER

www.elsevier.com/locate/ijhmt

Analysis of microchannel heat sinks for electronics cooling

C.Y. Zhao, T.J. Lu *

Department of Engineering, University of Cambridge, Trumpington Street, Cambridge CB2 1PZ, UK

Received 22 October 2001; received in revised form 25 February 2002

Abstract

This paper presents an analytical and numerical study on the heat transfer characteristics of forced convection across a microchannel heat sink. Two analytical approaches are used: the porous medium model and the fin approach. In the porous medium approach, the modified Darcy equation for the fluid and the two-equation model for heat transfer between the solid and fluid phases are employed. Firstly, the effects of channel aspect ratio (α_s) and effective thermal conductivity ratio ($\tilde{k}$) on the overall Nusselt number of the heat sink are studied in detail. The predictions from the two approaches both show that the overall Nusselt number (Nu) increases as α_s is increased and decreases with increasing $\tilde{k}$. However, the results also reveal that there exists significant difference between the two approaches for both the temperature distributions and overall Nusselt numbers, and the discrepancy becomes larger as either α_s or $\tilde{k}$ is increased. It is suggested that this discrepancy can be attributed to the indispensable assumption of uniform fluid temperature in the direction normal to the coolant flow invoked in the fin approach. The effect of porosity (ε) on the thermal performance of the microchannel is subsequently examined. It is found that whereas the porous medium model predicts the existence of an optimal porosity for the microchannel heat sink, the fin approach predicts that the heat transfer capability of the heat sink increases monotonically with the porosity. The effect of turbulent heat transfer within the microchannel is next studied, and it is found that turbulent heat transfer results in a decreased optimal porosity in comparison with that for the laminar flow. A new concept of microchannel cooling in combination with microheat pipes is proposed, and the enhancement in heat transfer due to the heat pipes is estimated. Finally, two-dimensional numerical calculations are conducted for both constant heat flux and constant wall temperature conditions to check the accuracy of analytical solutions and to examine the effect of different boundary conditions on the overall heat transfer.

1. Introduction

The high-power density and compactness of next generation electronics requires efficient cooling methods for heat dissipation in order to maintain the electronics at acceptable temperature levels, e.g., below 100 °C. Microchannel heat sinks as illustrated in Fig. 1 have emerged as one of the effective cooling techniques, apparently first proposed by Tuckerman and Pease [1,2] for electronics cooling. They built a water-cooled integral heat sink with microscopic flow channels, and demonstrated that extremely high-power density with a heat flux as high as 790 W/cm^2 could be dissipated.

Following the work of Tuckerman and Pease, much research has been conducted for microchannel heat sinks, as reviewed by Phillips [3]. In most of these studies, the fin approach is employed. As well known, the fin approach is an effective tool to analyse the transport of heat in a number of practical applications, and has been used recently to study the heat transfer properties of open-celled metal foam and honeycomb heat sinks [4–6]. However, because the fin approach is based upon the assumption that the fluid temperature is uniform in the direction perpendicular to coolant flow, the range of its validity is limited. Knight et al. [7] used empirical correlations to evaluate the performance of a microchannel heat sink, and found that its thermal resistance could be reduced by 35% compared to

* Corresponding author. Tel.: +44-1223-766316; fax: +44-1223-332662.

E-mail address: tjl21@cam.ac.uk (T.J. Lu).

0017-9310/02/$ - see front matter
PII: S0017-9310(02)00180-1

Nomenclature

a	width of channel
$\tilde{a}$	wetted area per volume
A	area
b	height of triangular grooves
Bi	Biot number $= ht/k_s$
$\tilde{Bi}$	equivalent Biot number in porous medium model, $h\tilde{a}H^2/(1-\varepsilon)k_s$
C_f	heat capacity of fluid
Da	Darcy number, K/H^2
D_h	hydraulic diameter of channel, $2ta/(t+a)$
h	interfacial heat transfer coefficient
$\overline{h}$	overall heat transfer coefficient
H	channel height
k_f	thermal conductivity of fluid
k_{fe}	effective thermal conductivity of fluid, εk_f
k_s	thermal conductivity of solid
k_{se}	effective thermal conductivity of solid, $(1-\varepsilon)k_s$
$\tilde{k}$	effective thermal conductivity ratio, $\varepsilon k_f/(1-\varepsilon)k_s$
K	permeability
L	length of heat sink
$\dot{m}$	mass flow rate
Nu_∞	interfacial Nusselt number for fully developed flow in microchannel, hD_h/k_f
$\overline{Nu}$	overall Nusselt number
$\overline{Nu}_{max}$	optimised overall Nusselt number
p	pressure
P	dimensionless pressure in porous medium approach
q_w	heat flux over bottom surface
s	pitch of triangular grooves
t	width of channel plate
T	temperature
T_0	inlet fluid temperature
T_L	outlet fluid temperature
T_w	bottom wall temperature
u	velocity
u_m	mean fluid velocity
U	dimensionless velocity
W	width of heat sink
Y	dimensionless vertical coordinate, y/H
$\langle\ \rangle_f$	volume-averaged value over fluid region
$\langle\ \rangle_s$	volume-averaged value over solid region

Greek symbols

α_s	aspect ratio of microchannel, H/a
ε	porosity
ε_{opt}	optimised porosity
ρ_f	density of fluid
θ_f	dimensionless temperature of fluid
θ_s	dimensionless temperature of solid
ϕ	angle of triangular grooves
μ_f	viscosity of fluid

Subscripts

b	bulk
f	fluid
m	mean value
s	solid
w	wall

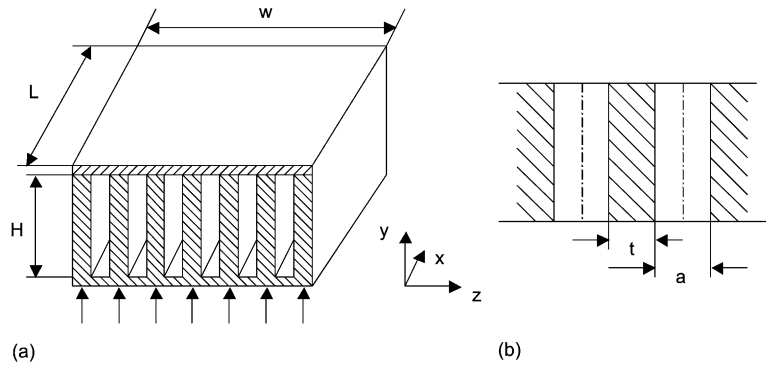

Fig. 1. Microchannel heat sink: geometry and definitions.

that obtained by Tuckerman and Pease with the fin approach [1].

On the other hand, Koh and Colony [8] modelled the microchannels as a porous medium by using Darcy's

law to describe the flow. More recently, Kim and Kim [9,10] analysed laminar heat transfer in microchannel heat sinks by using the modified Darcy model for fluid flow and two-equation model for heat transfer. The uniform fluid temperature assumption invoked in the fin approach is thus relaxed so that the temperature distributions of both solid and fluid along both the flow and transverse directions can be obtained. The analytical solutions of Kim and Kim [9,10] were shown to be in good agreement with the closed-form solution for the velocity distribution and the numerical solutions for the conjugate heat transfer problem. However, Kim and Kim did not carry out a systematic study on the effects of important parameters such as the channel aspect ratio, effective thermal conductivity ratio and porosity on the overall thermal performance of a microchannel heat sink, and their analysis is limited to laminar flow under the constant heat flux boundary condition. Furthermore, for the constant wall temperature boundary condition, it is difficult to solve the problem analytically based on the porous medium model, and hence a numerical approach is needed.

In a typical microchannel heat sink (Fig. 1), heat is removed mainly by conduction through solid and then dissipated away by interfacial convection. It is therefore expected that heat dissipation will be enhanced by increasing the solid conductivity. It is well known that microheat pipes are capable of dramatically enhancing the heat transfer in electronic devices. Cotter [11] is the first to introduce the concept of microheat pipe where the mean curvature of the vapour–liquid interface is of the same magnitude as the reciprocal of the hydraulic radius of the total flow channel. A microheat pipe is commonly defined as a wickless, noncircular channel with a hydraulic diameter of 10–500 μm and a length of about 10–20 mm. With recent development in micromanufacturing, microheat pipes can be fabricated on both surfaces of a microchannel by using, e.g., the vapour deposition technique [12,13]. A new type of heat sink combining microchannels and microheat pipes is therefore possible, and its heat transfer characteristics need to be studied.

The main objectives of the present paper are as follows: (1) compare the analytical solutions obtained with both the fin approach and the porous medium model, and hence examine the validity of the fin approach for microchannel heat sinks; (2) study the effects of channel aspect ratio (α_s), effective thermal conductivity ratio ($\bar{k}$) and porosity (ε) on the overall heat transfer coefficient of a microchannel heat sink, and obtain the optimal porosity for maximum heat dissipation; (3) estimate the effect of turbulent heat transfer; (4) calculate the heat transfer augmentation of the microchannel heat sink incorporating microheat pipes; (5) conduct two-dimensional (2-D) numerical calculations for two different boundary conditions—constant heat flux and constant wall temperature, and compare with the corresponding analytical solutions.

2. Problem definition

The problem considered is forced convective flow through a microchannel heat sink as shown in Fig. 1(a). Each channel has a height H, width a, length L, and the thickness of the channel plate is t, (see Fig. 1(b)). The direction of fluid flow is parallel to the x-axis. The bottom surface ($y = 0$) is kept either at constant temperature (T_w) or constant heat flux (q_w), and the top surface ($y = H$) is insulated. It is assumed that the width of the heat sink, W, is much larger than either a or t, and hence the focus of the analysis will be placed on a single channel. Furthermore, both the fluid temperature $T_f(x, y)$ and the solid plate temperature $T_s(x, y)$ are averaged over the width of the channel so that the problem can be effectively reduced to a 2-D one.

Fully developed heat and fluid flow are assumed in the analysis, and the thermal physical properties, e.g. thermal conductivity, density and viscosity, are taken to be temperature independent. The analysis will initially be limited to laminar heat transfer, but will be extended later to include the effect of turbulent flow due to surface roughness or high Reynolds numbers.

3. Fin approach

3.1. Constant wall temperature

The fin theory applied to the microchannel heat sink is actually a one-dimensional steady-state heat conduction problem with internal heat source [14]. The unit cell as shown in Fig. 1(b) by dashed lines is taken as the analytical domain, and it is assumed that the fluid temperature is averaged over the height of the microchannel, with $T_f = T_f(x)$, so the fluid temperature $T_f(x)$ is the bulk mean fluid temperature over the cross-section. According to the fin theory, the variation of the temperature T along the solid plate is governed by

$$\frac{d^2T}{dy^2} - \frac{2h}{k_s t}(T - T_f) = 0 \tag{1}$$

where h is the interfacial coefficient and k_s is the solid conductivity.

Subjected to the boundary condition $T = T_w$ at $y = 0$ and $dT/dy = 0$ at $y = H$, Eq. (1) can be solved to get

$$T(x, y) = T_f(x) + (T_w - T_f(x))\frac{\cosh\{\sqrt{2Bi}(H - y)/t\}}{\cosh(\sqrt{2Bi}H/t)} \tag{2}$$

where $Bi = ht/k_s$ is the Biot number. From Eq. (2) the average plate temperature is obtained as

$$\overline{T}(x) = T_f(x) + (T_w - T_f(x))\frac{\tanh\{\sqrt{2Bi}H/t\}}{\sqrt{2Bi}H/t} \tag{3}$$

Consequently, the total heat lost to the cooling medium per unit length of heat sink is

$$q(x) = -k_s t \left.\frac{dT}{dy}\right|_{y=0} = \sqrt{2Bi}k_s(T_w - T_f(x))\tanh\left(\sqrt{2Bi}\frac{H}{t}\right) \tag{4}$$

To complete the solution, the mean fluid temperature along the stream direction $T_f(x)$ needs to be solved. Note that the fin approach does not consider the fluid temperature variation in the transverse direction, whereas in reality the temperature of the fluid situated near the bottom plate is warmer than that farther away from it. As a result, the following energy balance equation is obtained

$$\dot{m}C_f\,dT_f(x) = [q(x) + q_{plate}]\,dx \tag{5}$$

where $\dot{m} = \rho_f a H u_m$ is the mass flow rate, and $q_{plate} = ha(T_w - T_f(x))$ is the heat flux per unit length from the bottom wall. From Eq. (5), the solution of the mean fluid temperature is obtained as

$$T_f(x) = T_w - (T_w - T_0)\exp\left(-\frac{x}{L^*}\right) \tag{6}$$

where

$$L^* = \frac{\rho_f C_f u_m H}{h}\left\{1 + \frac{t}{a}\sqrt{\frac{2}{Bi}}\tanh\left(\sqrt{2Bi}\frac{H}{t}\right)\right\}^{-1} \tag{7}$$

is the characteristic length scale of the problem. For efficient heat transfer, the microchannel heat sink should not be designed to be much longer than the characteristic length scale. From Eq. (6), the average fluid temperature inside the heat sink is obtained as

$$\overline{T}_f = T_0 + (T_w - T_0)\left\{1 - \frac{L^*}{L}[1 - \exp(-L/L^*)]\right\} \tag{8}$$

The overall heat transfer coefficient $\overline{h}$ of the microchannel heat sink can be defined as

$$\overline{h} = \frac{Q}{L(t+a)\Delta T_m} \tag{9}$$

where Q is the total heat transfer rate per channel:

$$Q = \rho_f u_m C_f Ha(T_f(L) - T_f(0)) = \rho_f u_m C_f Ha(T_w - T_0)\{1 - \exp(-L/L^*)\} \tag{10}$$

whereas ΔT_m is the logarithmic mean temperature difference:

$$\Delta T_m = \frac{(T_w - T_0) - (T_w - T_L)}{\ln[(T_w - T_0)/(T_w - T_L)]} \tag{11}$$

It can be easily verified from Eqs. (6), (8) and (11) that $\Delta T_m = T_w - \overline{T}_f$. The final expression for $\overline{h}$ is

$$\overline{h} = \frac{\rho_f u_m C_f Ha}{(t+a)L^*} = \frac{a}{t+a}h\left[1 + \frac{t}{a}\sqrt{\frac{2}{Bi}}\tanh\left(\sqrt{2Bi}\frac{H}{t}\right)\right] \tag{12}$$

3.2. Constant wall heat flux

For the constant wall heat flux boundary condition, with the assumption of uniform heat flux q_w in the direction normal to the bottom surface and thermal insulation at the top surface:

$$-k_s\left.\frac{dT}{dy}\right|_{y=0} = q_w \quad \text{and} \quad k_s\left.\frac{dT}{dy}\right|_{y=H} = 0$$

and by following the procedures outlined above for the case of constant wall temperature, the solution for the solid plate temperature can be obtained as:

$$T(x,y) = T_f(x) + \frac{q_w t}{k_s\sqrt{2Bi}}\frac{\cosh\{\sqrt{2Bi}(H-y)/t\}}{\sinh(\sqrt{2Bi}H/t)} \tag{13}$$

The average solid plate temperature along the vertical direction is

$$\overline{T}(x) = T_f(x) + \frac{q_w t}{2hH} \tag{14}$$

and the temperature difference between the solid plate and the coolant is

$$T_w(x) - T_f(x) = \frac{q_w t}{k_s\sqrt{2Bi}}\tanh^{-1}\left(\frac{\sqrt{2Bi}H}{t}\right) \tag{15}$$

By energy balance, the mean fluid temperature along the stream direction can be obtained as:

$$T_f(x) = T_0 + \frac{q_w(t+a)}{\rho_f a H u_m C_p}x \tag{16}$$

From Eq. (15), it is seen that the temperature difference between the plate and fluid is independent of x, an intrinsic feature of heat transfer in ducts with constant wall heat flux. Thus, the overall heat transfer coefficient $\overline{h}$ can be defined as

$$\overline{h} = \frac{q_w}{(T_w(x) - T_f(x))} \tag{17a}$$

Substitution of Eqs. (15) and (16) into Eq. (17a) results in:

$$\overline{h} = \frac{k_s\sqrt{2Bi}}{t}\tanh\left(\frac{\sqrt{2Bi}H}{t}\right) \tag{17b}$$

3.3. Interfacial heat transfer coefficient

It should be noted that the interfacial heat transfer coefficient (h) appearing in the above solutions is yet to be determined. For fully developed channel flow, accurate correlations of h for laminar heat transfer are available in the open literature. In the present investigation, the correlation in terms of channel aspect ratios (α_s) obtained by Kim and Kim [9] will be employed, which is given by

$$Nu_\infty = \frac{hD_h}{k_f} = 2.253 + 8.164\left(\frac{\alpha_s}{\alpha_s + 1}\right)^{1.5} \quad \text{for } Re < 2000 \tag{18}$$

4. Porous medium model

Up to now, the heat transfer of a microchannel heat sink for both constant heat flux and constant wall temperature boundary conditions have been investigated by using the fin approach, leading to analytical solutions for the overall heat transfer coefficient and temperature distributions. As previously discussed, the fin approach assumes constant fluid temperature along the height of the channel wall. In the following section, this assumption will be relaxed and the analytical solution for constant heat flux boundary condition will be obtained by using porous media approach. However, for the case of constant wall temperature, an analytical solution is difficult, if not impossible, to obtain, and hence will be solved later by using the numerical method described in Section 5.

The approach is similar to that used by Kim and Kim [9,10] and hence only a few important equations will be listed for reference. The extended Darcy equation proposed by Vafai and Tien [15] for fluid flow and the volume-averaged two-equation model [16] for heat transfer are used. The governing equations and the corresponding boundary conditions are

$$-\frac{d}{dx}\langle p\rangle_f + \mu_f \frac{d^2}{dy^2}\langle u\rangle_f - \frac{\mu_f}{K}\varepsilon\langle u\rangle_f = 0 \tag{19}$$

$$k_{se}\frac{\partial^2\langle T\rangle_s}{\partial y^2} = h\tilde{a}(\langle T\rangle_s - \langle T\rangle_f) \tag{20}$$

$$\varepsilon\rho_f C_f\langle u\rangle_f\frac{\partial\langle T\rangle_f}{\partial x} = h\tilde{a}(\langle T\rangle_s - \langle T\rangle_f) + k_{fe}\frac{\partial^2\langle T\rangle_f}{\partial y^2} \tag{21}$$

$$\langle u\rangle_f = 0 \quad \text{at } y = 0, H \tag{22}$$

$$\langle T\rangle_s = \langle T\rangle_f = T_w \quad \text{at } y = 0 \tag{23}$$

$$\frac{\partial\langle T\rangle_s}{\partial y} = \frac{\partial\langle T\rangle_f}{\partial y} = 0 \quad \text{at } y = H \tag{24}$$

where $\langle\ \rangle$ represents a volume-averaged value, and k_{se}, $T, h, \tilde{a}, \rho_f, C_f$ and k_{fe} are effective thermal conductivity of the solid, temperature, interfacial heat transfer coefficient, wetted area per volume, density, heat capacity and effective thermal conductivity of the fluid, respectively. For the microchannel heat sink shown in Fig. 1, the porosity, permeability, and effective conductivities can be written as

$$\varepsilon = \frac{a}{a+t}, \quad K = \frac{\varepsilon a^2}{12}, \quad k_{se} = (1-\varepsilon)k_s, \quad k_{fe} = \varepsilon k_f \tag{25}$$

Eqs. (19)–(21) can be nondimensionalised by introducing the following variables:

$$U = \frac{\langle u\rangle_f}{u_m}, \quad Da = \frac{K}{H^2}, \quad Y = \frac{y}{H}, \quad P = \frac{K}{\varepsilon\mu_f u_m}\frac{d\langle p\rangle_f}{dx},$$
$$\theta_s = \frac{\langle T\rangle_s - \langle T\rangle_w}{q_w H/(1-\varepsilon)k_s}, \quad \theta_f = \frac{\langle T\rangle_f - \langle T\rangle_w}{q_w H/(1-\varepsilon)k_s} \tag{26}$$

On the other hand, for fully developed flow subjected to a constant heat flux, it is known that:

$$\frac{\partial\langle T\rangle_f}{\partial x} = \frac{\partial\langle T\rangle_s}{\partial x} = \frac{dT_w}{dx} = \text{constant} \tag{27}$$

and, from energy balance,

$$q_w = \varepsilon\rho_f C_f u_m H\frac{\partial\langle T\rangle_f}{\partial x} \tag{28}$$

In summary, the nondimensionalised governing equations and boundary conditions are given by:

$$U = \frac{Da}{\varepsilon}\frac{d^2U}{dY^2} - P \tag{29}$$

$$\frac{d^2\theta_s}{dY^2} = \tilde{B}i(\theta_s - \theta_f) \tag{30}$$

$$U = \tilde{B}i(\theta_s - \theta_f) + \frac{\varepsilon k_f}{(1-\varepsilon)k_s}\frac{d^2\theta_f}{dY^2} \tag{31}$$

$$U = \theta_s = \theta_f = 0 \quad \text{at } Y = 0 \tag{32}$$

$$U = \frac{d\theta_s}{dY} = \frac{d\theta_f}{dY} = 0 \quad \text{at } Y = 1 \tag{33}$$

where $\tilde{B}i = h\tilde{a}H^2/(1-\varepsilon)k_s$.

From Eqs. (29), (32) and (33), the velocity distribution in the heat sink is obtained as:

$$U = P\cosh\left(\sqrt{\frac{\varepsilon}{Da}}Y\right) + P\frac{1-\cosh\left(\sqrt{\frac{\varepsilon}{Da}}\right)}{\sinh\left(\sqrt{\frac{\varepsilon}{Da}}\right)} \times \sinh\left(\sqrt{\frac{\varepsilon}{Da}}Y\right) - P \tag{34}$$

Since $\int_0^1 U\,dY = 1$, one obtains from Eq. (34) that

$$P=\frac{\sinh\left(\sqrt{\frac{\varepsilon}{Da}}\right)}{2\sqrt{\frac{Da}{\varepsilon}}\left\{\cosh\left(\sqrt{\frac{\varepsilon}{Da}}\right)-1\right\}-\sinh\left(\sqrt{\frac{\varepsilon}{Da}}\right)} \tag{35}$$

Now, because $\mathrm{d}\langle p\rangle/\mathrm{d}x=12\mu_{\mathrm{f}}u_{\mathrm{m}}P/a^2$, it follows from Eq. (35) that

$$\Delta\langle p\rangle=\int_0^L\frac{12\mu_{\mathrm{f}}u_{\mathrm{m}}P}{a^2}\,\mathrm{d}x=\frac{12\mu_{\mathrm{f}}u_{\mathrm{m}}P}{a^2}L \tag{36}$$

from which the friction factor is obtained as

$$f=\frac{\Delta\langle p\rangle D_h}{L\rho_{\mathrm{f}}u_{\mathrm{m}}^2/2}=\frac{96P}{Re}\left(\frac{\alpha_{\mathrm{s}}}{1+\alpha_{\mathrm{s}}}\right)^2 \tag{37}$$

Upon substitution of the velocity solution Eq. (34) into Eqs. (30) and (31) and after some tedious manipulations by following the procedures of Kim and Kim [9], the final temperature solutions for both the solid and fluid phases are obtained as:

$$\begin{aligned}\theta_{\mathrm{f}}=\frac{P}{1+\tilde{k}}\Bigg[&-\frac{1}{2}Y^2+C_1Y+C_6\\&-C_3\cosh\left(\sqrt{\frac{\tilde{Bi}\left(1+\tilde{k}\right)}{\tilde{k}}}Y\right)\\&-C_4\sinh\left(\sqrt{\frac{\tilde{Bi}\left(1+\tilde{k}\right)}{\tilde{k}}}Y\right)\Bigg]\\&+\frac{PC_7}{1+\tilde{k}}\Bigg[\Bigg\{\cosh\left(\sqrt{\frac{\varepsilon}{Da}}Y\right)\\&+\frac{1-\cosh\left(\sqrt{\frac{\varepsilon}{Da}}\right)}{\sinh\left(\sqrt{\frac{\varepsilon}{Da}}\right)}\sinh\left(\sqrt{\frac{\varepsilon}{Da}}Y\right)\Bigg\}\Bigg]\end{aligned} \tag{38}$$

$$\begin{aligned}\theta_{\mathrm{s}}=P\Bigg[&\frac{Da}{\varepsilon}\Bigg\{\cosh\left(\sqrt{\frac{\varepsilon}{Da}}Y\right)\\&+\frac{1-\cosh\left(\sqrt{\frac{\varepsilon}{Da}}\right)}{\sinh\left(\sqrt{\frac{\varepsilon}{Da}}\right)}\sinh\left(\sqrt{\frac{\varepsilon}{Da}}Y\right)\Bigg\}-\frac{1}{2}Y^2\\&+C_1Y+C_2\Bigg]-\tilde{k}\theta_{\mathrm{f}}\end{aligned} \tag{39}$$

where

$$\tilde{k}=\frac{\varepsilon k_{\mathrm{f}}}{(1-\varepsilon)k_{\mathrm{s}}},\quad C_1=1-\frac{\sqrt{Da/\varepsilon}(\cosh(\sqrt{\varepsilon/Da}-1))}{\sinh(\sqrt{\varepsilon/Da})}$$

$$D_1=\tilde{Bi}(1+\tilde{k})-\tilde{k}\varepsilon/Da,\quad C_2=\frac{-Da}{\varepsilon},\quad C_3=\frac{-\tilde{k}\frac{\varepsilon}{Da}}{[\tilde{Bi}(1+\tilde{k})D_1]}$$

$$C_4=\frac{(N_1+N_2)}{\left[\tilde{Bi}(1+\tilde{k})\sqrt{\tilde{Bi}(1+\tilde{k})/\tilde{k}}\cosh\left(\sqrt{\tilde{Bi}(1+\tilde{k})/\tilde{k}}\right)\sinh(\sqrt{\varepsilon/Da})D_1\right]}$$

$$C_5=\frac{1}{D_1},\quad C_6=\frac{-Da}{\varepsilon}+\frac{1}{[\tilde{Bi}(1+\tilde{k})]},\quad C_7=\frac{Da}{\varepsilon}-\frac{1}{D_1}$$

$$N_1=\tilde{Bi}(1+\tilde{k})\sqrt{\varepsilon/Da}\{1-\cosh(\sqrt{\varepsilon/Da})\}$$

$$N_2=\frac{\tilde{k}\varepsilon}{Da\sqrt{\tilde{Bi}(1+\tilde{k})/\tilde{k}}\sinh(\sqrt{\varepsilon/Da})\sinh\left(\sqrt{\tilde{Bi}(1+\tilde{k})/\tilde{k}}\right)}$$

Note that the local heat transfer coefficient h appearing in the above coefficients is still given by Eq. (18).

Finally, the overall heat transfer coefficient is obtained as

$$\bar{h}=\frac{q_{\mathrm{w}}}{T_{\mathrm{w}}(x)-T_{\mathrm{f,b}}(x)}=-\frac{(1-\varepsilon)k_{\mathrm{s}}}{H\theta_{\mathrm{f,b}}(x)} \tag{40}$$

where $\theta_{\mathrm{f,b}}(x)$ is the bulk mean fluid temperature averaged along the cross section of the channel, given by

$$\theta_{\mathrm{f,b}}(x)=\frac{T_{\mathrm{f,b}}(x)-T_{\mathrm{w}}(x)}{q_{\mathrm{w}}H/(1-\varepsilon)k_{\mathrm{s}}}=\frac{\int_0^1U\theta_{\mathrm{f}}\,\mathrm{d}Y}{\int_0^1U\,\mathrm{d}Y} \tag{41}$$

The overall Nusselt number for the microchannel heat sink is:

$$\overline{Nu}=\frac{\bar{h}H}{k_{\mathrm{f}}}=-\frac{(1-\varepsilon)k_{\mathrm{s}}}{k_{\mathrm{f}}\theta_{\mathrm{f,b}}} \tag{42}$$

5. Numerical analysis

So far, the analytical solution based on porous medium approach has been obtained only for the constant heat flux boundary condition. However, in order to simplify the problem so that an analytical solution can be obtained, those terms representing conduction in the stream direction have been neglected in the energy equations. Furthermore, for the constant wall temperature boundary condition, it is very difficult to solve the problem analytically, even if the axial conduction terms are ignored. Consequently, it is necessary to conduct full numerical calculations in order to check the accuracy of the analytical solutions and to solve the problem associated with constant wall temperature boundary conditions.

In the present numerical calculation, a fully developed velocity field is assumed and hence the momentum Eq. (19) remains unchanged, whereas the energy equations (20) and (21) are modified as:

$$0 = \frac{\partial}{\partial x}\left(k_{se}\frac{\partial T_s}{\partial x}\right) + \frac{\partial}{\partial y}\left(k_{se}\frac{\partial T_s}{\partial y}\right) - h_{sf}\tilde{a}(T_s - T_f) \tag{43}$$

$$\varepsilon\rho_f C_f u\frac{\partial T_f}{\partial x} = \frac{\partial}{\partial x}\left(k_{fe}\frac{\partial T_f}{\partial x}\right) + \frac{\partial}{\partial y}\left(k_{fe}\frac{\partial T_f}{\partial y}\right) + h_{sf}\tilde{a}(T_s - T_f) \tag{44}$$

The first term on the right hand side of Eqs. (43) and (44) is the contribution from axial conduction previously ignored. For brevity, the bracket $\langle\ \rangle$ representing volume averaging has been dropped in these equations. The boundary conditions are specified as follows:

$$q = q_w = k_{fe}\frac{\partial T_f}{\partial y}\bigg|_{y=0} + k_{se}\frac{\partial T_s}{\partial y}\bigg|_{y=0} \tag{45a}$$

$$T_s = \begin{cases} T_f, \text{ at } y = 0 & \text{constant heat flux} \\ T_f = T_w, \text{ at } y = 0 & \text{constant wall temperature} \end{cases} \tag{45b}$$

$$q = 0 \quad \text{at } y = H \tag{45c}$$

$$T_f = T_0 \quad \text{and} \quad \frac{\partial T_s}{\partial x} = 0 \quad \text{at } x = 0 \tag{45d}$$

$$\frac{\partial T_s}{\partial x} = 0 \quad \text{and} \quad \frac{\partial T_f}{\partial x} = 0 \quad \text{at } x = L \tag{45e}$$

The above 2-D heat transfer problem is solved by using the ADI finite difference scheme, with 127×46 uniform grid spacings used in the x- and y-directions, respectively. The convergence criterion is that the change in the solid-phase and fluid-phase temperatures is less than 10^{-5} between successive iterations.

6. Results and discussion

In order to compare the analytical solutions from the two different approaches, Eqs. (13)–(16) derived from the fin approach need to be nondimensionalised in the same way as those in the porous medium approach. Thus, the analytical solutions from the fin approach are rearranged as follows:

$$\theta_s(Y) = \frac{(1-\varepsilon)^2}{\varepsilon\alpha_s\sqrt{2Bi}} \times \frac{\cosh\left(\sqrt{2Bi}\frac{\varepsilon\alpha_s}{1-\varepsilon}(1-Y)\right) - \cosh\left(\sqrt{2Bi}\frac{\varepsilon\alpha_s}{1-\varepsilon}\right)}{\sinh\left(\sqrt{2Bi}\frac{\varepsilon\alpha_s}{1-\varepsilon}\right)} \tag{46}$$

$$\theta_f = -\frac{(1-\varepsilon)^2}{\varepsilon\alpha_s\sqrt{2Bi}}\frac{\cosh\left(\sqrt{2Bi}\frac{\varepsilon\alpha_s}{1-\varepsilon}\right)}{\sinh\left(\sqrt{2Bi}\frac{\varepsilon\alpha_s}{1-\varepsilon}\right)} \tag{47}$$

$$\overline{Nu} = \frac{\varepsilon\alpha_s}{1-\varepsilon}\frac{k_s}{k_f}\sqrt{2Bi}\tanh\left(\sqrt{2Bi}\frac{\varepsilon\alpha_s}{1-\varepsilon}\right) \tag{48}$$

Note that the Biot number Bi appearing in the above equations for the fin approach is related to the effective thermal conductivity ratio ($\tilde{k}$), local Nusselt number (Nu_∞), porosity (ε), and aspect ratio (α_s) by

$$Bi = \frac{ht}{k_s} = \frac{\tilde{B}i}{2\left(\frac{\varepsilon}{1-\varepsilon}\right)^2\alpha_s^2} = \frac{\tilde{k}Nu_\infty(\alpha_s+1)}{2\left(\frac{\varepsilon}{1-\varepsilon}\right)^2\alpha_s} \tag{49}$$

6.1. Effect of channel aspect ratio (α_s)

For fixed values of effective thermal conductivity ratio ($\tilde{k} = 0.004$) and porosity ($\varepsilon = 0.5$), Figs. 2 and 3 show the nondimensional solid and fluid temperature distributions predicted from the fin approach and the porous medium model, for two different aspect ratios, $\alpha_s = 2$ and 10, respectively. For the solid temperature, both approaches predict, correctly, that the solid temperature decreases from the heated bottom wall to the insulated top wall. However, it is seen from Figs. 2(a) and 3(a) that the discrepancy between the two predictions is large, and this discrepancy increases as the aspect ratio α_s is increased. On the other hand, for the fluid temperature, Figs. 2(b) and 3(b) show different trends for the two approaches. The fin approach leads to a constant temperature distribution in the transverse direction of the channel, whilst the porous medium approach predicts that the fluid temperature first decreases sharply from its maximum value at the bottom wall,

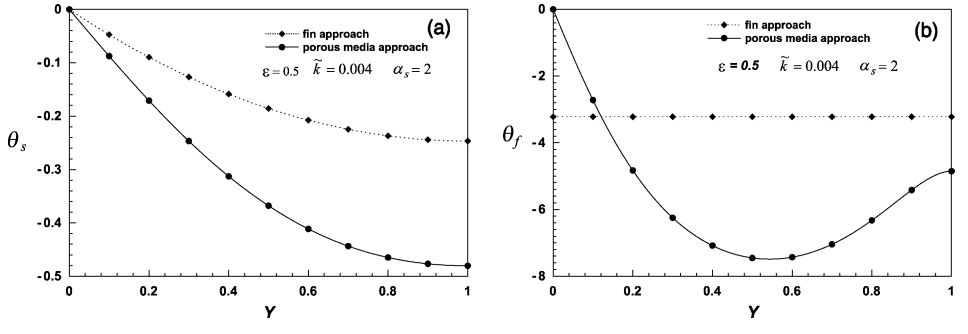

Fig. 2. Dimensionless temperature distributions for $\alpha_s = 2$, $\varepsilon = 0.5$ and $\tilde{k} = 0.004$: (a) solid; (b) fluid.

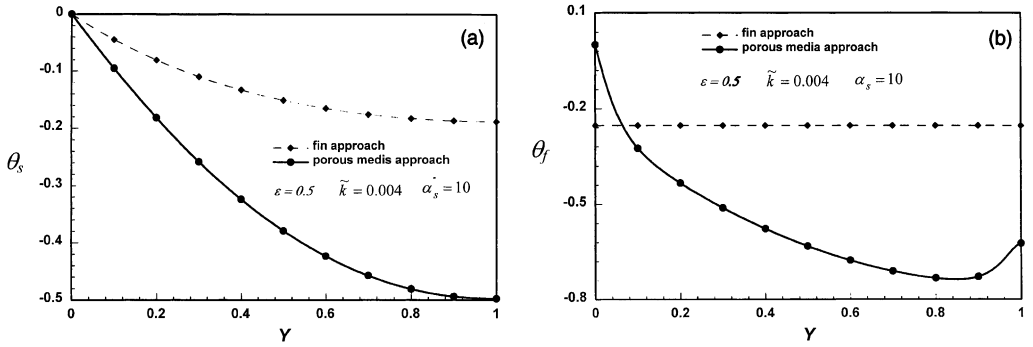

Fig. 3. Dimensionless temperature distribution for $\alpha_s = 10$, $\varepsilon = 0.5$ and $\tilde{k} = 0.004$: (a) solid; (b) fluid.

reaches a minimum, and then increases gradually due to the effect of the top wall temperature. Kim and Kim [9] have shown that the temperature distribution predicted by the porous medium approach is accurate in comparison with the numerical solutions to within 4.0%. Our own numerical simulation (see Sections 5 and 6.6) has also confirmed that the porous medium approach yields accurate predictions. Therefore, it may be concluded that the large discrepancy exhibited by the results of the fin approach from those of the porous medium approach is attributable to the constant fluid temperature assumption invoked by the fin approach.

Fig. 4 shows the effect of α_s on the overall Nusselt number for $\tilde{k} = 0.004$ and $\varepsilon = 0.5$. Both approaches predict that the overall Nusselt number increases with increasing aspect ratio (α_s), although the predicted value from the fin approach is approximately twice that of the porous medium approach for a given α_s. In other words, the assumption of constant fluid temperature by the fin approach leads to an overestimation of the heat transfer performance for microchannel heat sinks.

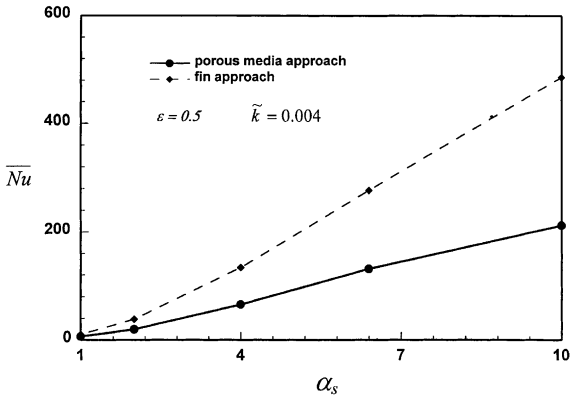

Fig. 4. Overall Nusselt number plotted as a function of channel aspect ratio α_s for $\varepsilon = 0.5$ and $\tilde{k} = 0.004$.

6.2. Effect of thermal conductivity ratio($\tilde{k}$)

For a given aspect ratio ($\alpha_s = 10$) and porosity ($\varepsilon = 0.5$), the solid and coolant temperature distributions are presented in Figs. 5 and 6, for $\tilde{k} = 0.001$ and 0.01, respectively. Again, a large discrepancy exists between the results from the two different approaches, increasing as the thermal conductivity ratio is increased. With $\alpha_s = 10$ and $\varepsilon = 0.5$, the overall Nusselt number is plotted as a function of the thermal conductivity ratio in Fig. 7. It is seen that both approaches predict that $\overline{Nu}$ decreases with increasing $\tilde{k}$, but the prediction from the fin approach is about twice that by the porous medium approach.

6.3. Effect of porosity (ε)

For any microchannel heat sink design, it is important to know if an optimal porosity exists for maximum heat dissipation and, if it does exist, how it varies with the Reynolds number, geometrical parameters such as the channel aspect ratio, and mode of heat transfer (laminar versus turbulent). Fig. 8 plots the overall Nusselt number as a function of porosity for $\alpha_s = 10$ and $\tilde{k} = 0.004$. Whilst the fin approach predicts that $\overline{Nu}$ increases monotonically with ε, the porous medium approach predicts that $\overline{Nu}$ reaches its maximum when $\varepsilon \cong 0.42$. However, this optimal porosity is not independent of channel aspect ratio and thermal conductivity ratio. With $\tilde{k} = 0.004$, Fig. 9 presents the variation of $\overline{Nu}$ with porosity for three aspect ratios: $\alpha_s = 10$, 5 and 1. It is seen that the optimal porosity increases as α_s is reduced. Fig. 10 plots the optimised porosity ε_{opt} as a function of α_s for $\tilde{k} = 0.004$. It is seen that the optimised porosity decreases nearly linearly with increasing α_s, with $\varepsilon_{opt} = 0.9$ at $\alpha_s = 1$ and $\varepsilon_{opt} = 0.5$ at $\alpha_s = 10$. With $\overline{Nu}_{max}$ representing the overall Nusselt number of a microchannel heat sink designed at the optimal porosity, Fig. 11 presents the variation of

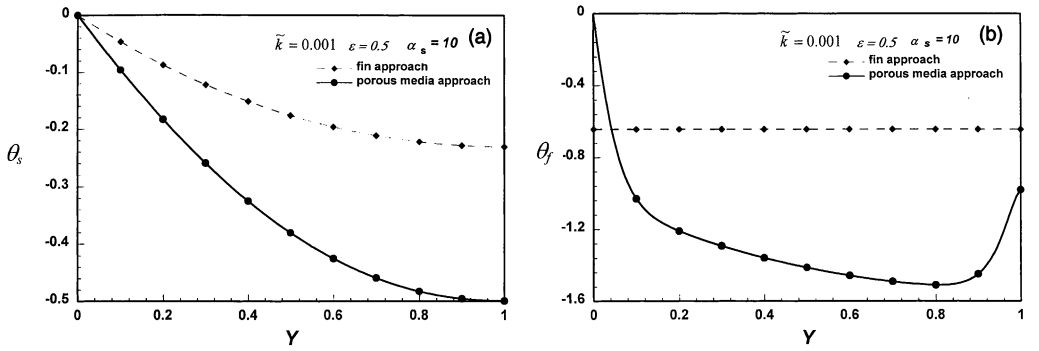

Fig. 5. Dimensionless temperature distributions for $\alpha_s = 10$, $\varepsilon = 0.5$ and $\tilde{k} = 0.001$: (a) solid; (b) fluid.

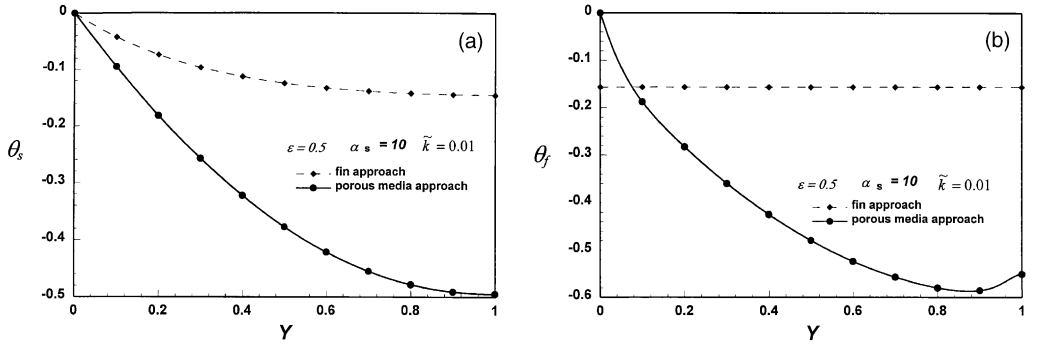

Fig. 6. Dimensionless temperature distributions for $\alpha_s = 10$, $\varepsilon = 0.5$ and $\tilde{k} = 0.01$: (a) solid; (b) fluid.

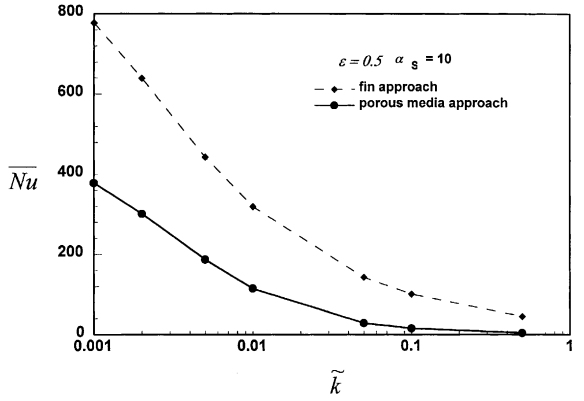

Fig. 7. Overall Nusselt number plotted as a function of effective thermal conductivity ratio $\tilde{k}$ for $\varepsilon = 0.5$ and $\alpha_s = 10$.

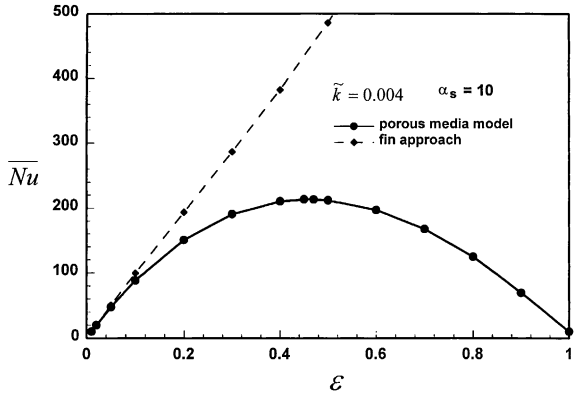

Fig. 8. Overall Nusselt number plotted as a function of porosity for $\tilde{k} = 0.004$ and $\alpha_s = 10$.

$\overline{Nu}_{max}$ with α_s for $\tilde{k} = 0.004$. Again, $\overline{Nu}_{max}$ is approximately a linear function of α_s, and the value of $\overline{Nu}_{max}$ increases from about 10 at $\alpha_s = 1$ to about 210 at $\alpha_s = 10$.

Fig. 12 presents the heat transfer efficiency factor $\tilde{J}_{max}/f$ as a function of the channel aspect ratio for $\tilde{k} = 0.004$. Here, f is the friction factor defined in Eq. (37), and $\tilde{J}_{max} = \overline{Nu}_{max}/Re$ is the modified j-Colburn factor corresponding to the optimised porosity. The thermal efficiency of a microchannel heat sink is seen from Fig. 12 to increase linearly as the channel aspect ratio is increased.

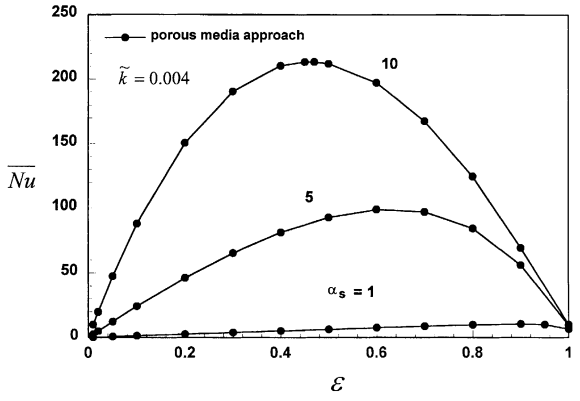

Fig. 9. Overall Nusselt number plotted as a function of porosity for $\tilde{k} = 0.004$ and selected values of α_s.

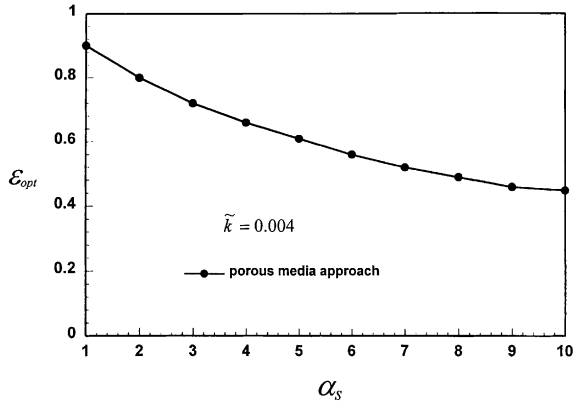

Fig. 10. Optimised porosity (ε_{opt}) plotted as a function of channel aspect ratio (α_s) for $\tilde{k} = 0.004$.

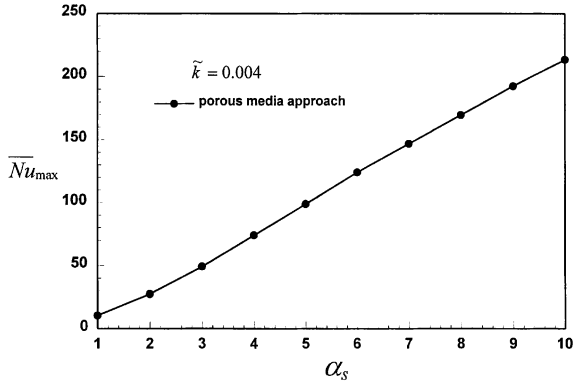

Fig. 11. Maximum overall Nusselt number plotted as a function of channel aspect ratio (α_s) for $\tilde{k} = 0.004$.

6.4. Effect of turbulence heat transfer

In this section, the effect of turbulence on microchannel heat transfer is considered. Turbulence in the channel may be induced by surface roughness and/or high Reynolds numbers. Strictly speaking, the inertia term should be included in the momentum equation (19) to account for the turbulence effect on coolant velocity. In the present study, however, the effect of turbulence on heat transfer will be calculated approximately, and its effect on velocity distribution will not be examined. Furthermore, the effect of thermal diffusion on the overall transport is considered negligible, because the dominant mode of transport is by conduction through the solid phase and interfacial convection, which is largely unaffected by dispersion. Thus, the turbulence effect can be considered by modifying the interfacial heat transfer coefficient, h; the rest of the governing equations and boundary conditions remain unchanged as in the laminar case. The fully developed turbulent heat transfer in a microchannel can be correlated as [7]:

$$Nu_\infty = \frac{hD_h}{k_f} = 0.040 Re^{3/4} \mathrm{Pr}^{1/3} \quad \text{for } Re \geqslant 2000 \tag{50}$$

Fig. 13 shows the variation of $\overline{Nu}$ with Re for $\tilde{k} = 0.004$, $\alpha_s = 10$ and $\varepsilon = 0.5$; predictions from both the fin ap-

Fig. 12. Optimised thermal efficiency factor plotted as a function of channel aspect ratio (α_s) for $\tilde{k} = 0.004$.

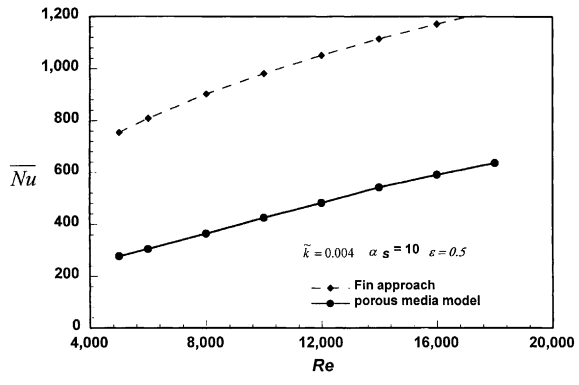

Fig. 13. Variation of $\overline{Nu}$ with Re for turbulent heat transfer, with $\tilde{k} = 0.004$, $\alpha_s = 10$ and $\varepsilon = 0.5$.

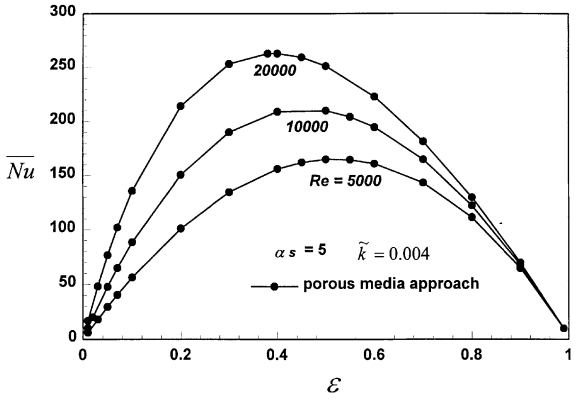

Fig. 14. Variation of $\overline{Nu}$ with porosity for selected values of Reynolds number, with $\tilde{k} = 0.004$, $\alpha_s = 5$.

proach and the porous medium model are included. The effect of porosity on $\overline{Nu}$ is presented in Fig. 14 for selected values of Re, with $\tilde{k} = 0.004$ and $\alpha_s = 10$. Only the predictions from the porous medium model are shown in Fig. 14, and it is seen that the optimised porosity decreases as the Reynolds number is increased. The comparison of the optimised porosity between laminar and turbulent flow is shown in Fig. 15 for $\tilde{k} = 0.004$. For a fixed channel aspect ratio α_s, the optimised porosity decreases by about 20% when the flow changes from laminar to turbulent.

6.5. Microchannel heat sink in combination with microheat pipes

With the vapour deposition technique [12,13], a series of small triangular grooves can be fabricated onto the channel wall as illustrated in Fig. 16, allowing an array of miro heat pipes to be constructed. The heat transfer in microheat pipes involves the liquid–vapour phase change, and its analysis is complicated. In this paper, by

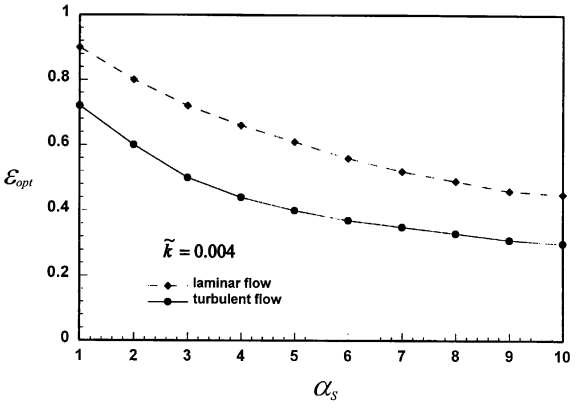

Fig. 15. Optimised porosity (ε_{opt}) as a function of channel aspect ratio: effect of heat transfer mode.

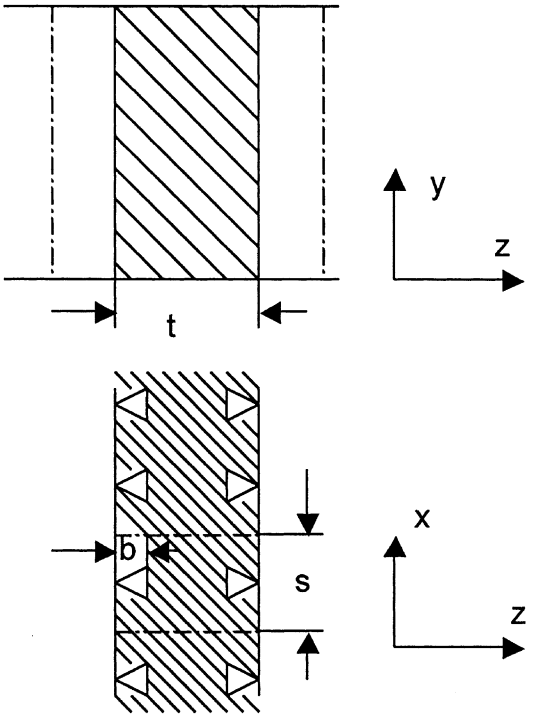

Fig. 16. Triangular grooves on both sides of channel wall as microheat pipes.

using a lumped capacitance technique, the microheat pipes are modelled as homogeneous, solid regions embedded in the plates with an effective thermal conductivity k_{pipe}. The effective thermal conductivity of a microheat pipe is assumed to be $\approx$10 times that of copper or silicon [13,14]. With the assumption that the microheat pipes are arranged periodically along the x-direction and the temperature across the thickness of the plate (t) is uniform, the equivalent solid conductivity of the channel wall incorporating the microheat pipes can be obtained as follows:

$$k_{s,eq} = \frac{A_{pipe}}{A} k_{pipe} + \frac{A_s}{A} k_s = \frac{2b^2}{st} \tan\frac{\phi}{2} k_{pipe} + \left(1 - \frac{2b^2}{st} \tan\frac{\phi}{2}\right) k_s \quad (51)$$

where ϕ is the angle of the triangular groove of the heat pipe. If it is further assumed that $A_{pipe}/A = 0.1$ and $k_s/k_f = 1000$, one finds from (51) that $k_{s,eq}/k_f = 2400$. The porous medium model is used to complete the analysis. The comparison of the overall heat transfer is shown in Fig. 17(a) for microchannels with and without microheat pipes. It can be seen that the enhancement in heat transfer due to the incorporation of heat pipes becomes significant as the channel aspect ratio increases. If the solid-to-fluid conductivity ratio is reduced to $k_s/k_f = 100$, corresponding to the case of high

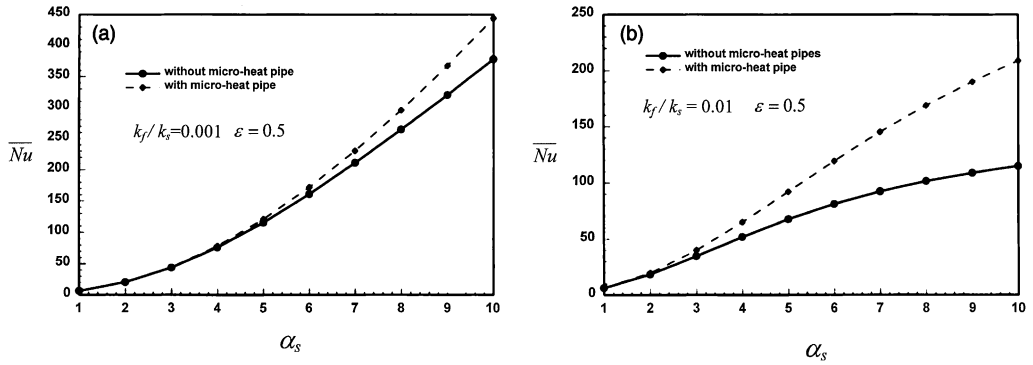

Fig. 17. Effect of microheat pipes on overall Nusselt number as a function of channel aspect ratio: (a) $k_f/k_s = 0.001$; (b) $k_f/k_s = 0.01$.

conducting coolant such as water, the effect of heat pipes becomes more significant, as shown in Fig. 17(b). For example, at $\alpha_s = 10$, the heat transfer capability of the microchannel heat sink is nearly doubled due to microheat pipes. The effect will be more pronounced as the cross-sectional area of the channel wall occupied by the microheat pipes is increased.

6.6. Numerical simulation

It should be pointed out that above analytical solutions are based on the assumption that the effect of axial conduction is negligibly small. In order to verify that this assumption is reasonable, 2-D numerical calculations as outlined in Section 5 are conducted. The comparison between the analytical and numerical results is plotted in Fig. 18. It can be seen that the agreement between the analytical solutions and numerical results is very good. It indicates that analytical solutions based on the porous medium approach can give explicit and accurate predictions for the case of constant heat flux. The same conclusion is reached by Kim and Kim [9].

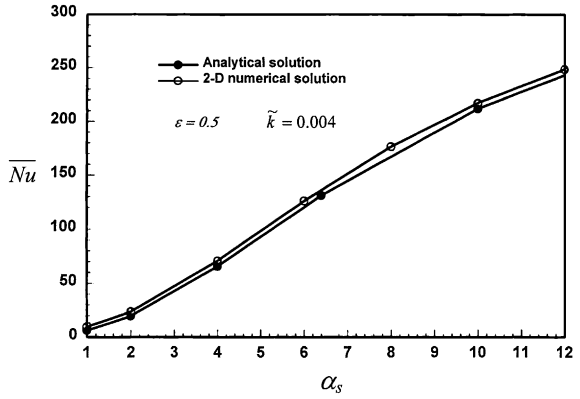

Fig. 18. Overall Nusselt number as a function of channel aspect ratio: analytical modelling versus numerical calculation for $\varepsilon = 0.5$ and $\tilde{k} = 0.004$.

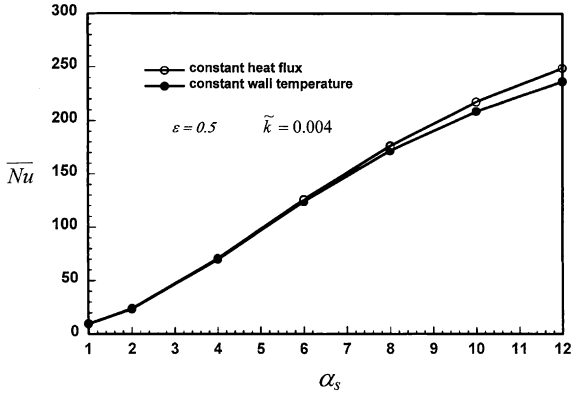

Fig. 19. Overall Nusselt number as a function of channel aspect ratio: effect of heat transfer boundary conditions for $\varepsilon = 0.5$ and $\tilde{k} = 0.004$.

6.7. Constant heat flux versus constant wall temperature

For the constant wall temperature boundary condition, it is very difficult to solve the heat transfer problem analytically by using the porous medium approach, and hence 2-D numerical calculations have been conducted. Fig. 19 shows the comparison of the results between the two different boundary conditions, with $\varepsilon = 0.5$ and $\tilde{k} = 0.004$. Overall, the difference between the two sets of results is small, with the overall Nusselt number from the constant heat flux condition slightly higher than that from the constant wall temperature condition for larger channel aspect ratios ($\alpha_s > 8$).

7. Conclusions

In this paper, the heat transfer performance of microchannel heat sinks has been analysed by using the fin approach and the porous medium approach. The results shows that the fin approach significantly overestimates the heat transfer due to the assumption of constant fluid

temperature in the direction perpendicular to coolant flow. The analytical solution based on the porous medium approach agrees excellently with 2-D numerical calculations. Furthermore, unlike the porous medium model, the fin approach fails to predict the existence of an optimal porosity, and hence is deemed unsuitable for designing microchannel heat sinks. The optimised porosity (ε_{opt}) decreases as the channel aspect ratio (α_s) increases or if the mode of heat transfer is changed from laminar to turbulent. It is also found that microchannel heat sinks incorporating microheat pipes have significantly higher heat transfer capabilities in comparison to those without, particularly if the channel aspect ratio is relatively large and the coolant is a high conducting liquid instead of air. The study shows that the effect of heat transfer boundary conditions (constant heat flux versus constant wall temperature) on the overall Nusselt number of a microchannel heat sink is small.

Acknowledgements

This work is supported partially by the U.S. Office of Naval Research (ONR/ONRIFO grant number N000140110271), partially by the U.S. DAPRA/ONR MURI program on Ultralight Metal Structures (no. N00014-1-96-1028), and partially by the U.K. Engineering and Physical Sciences Research Council (EPSRC grant number EJA/U83).

References

[1] D.B. Tuckerman, R.F.W. Pease, High-performance heat sinking for VLSI, IEEE Electron Dev. Lett. 2 (1981) 126–129.
[2] D.B. Tuckerman, R.F.W. Pease, Ultrahigh thermal conductance microstructures for integrated circuits, in: IEEE Proc. 32nd Electronics Conference, 1982, pp. 145–149.
[3] R.J. Philips, Micro-channel heat sinks, in: A. Bar-Cohen, A.D. Kraus (Eds.), Advances in Thermal Modelling of Electronic Components and Systems, vol. 2, ASME, New York, 1990 (Chapter 3).
[4] T.J. Lu, H.A. Stone, M.F. Ashby, Heat transfer in open-cell metal foams, Acta Mater. 46 (1998) 3619–3635.
[5] T.J. Lu, Heat transfer efficiency of metal honeycombs, Int. J. Heat Mass Transfer 42 (1999) 2031–2040.
[6] S. Gu, T.J. Lu, A.G. Evans, On the design of two-dimensional cellular metals for combined heat dissipation and structural load capacity, Int. J. Heat Mass Transfer 44 (2001) 2163–2175.
[7] R.W. Knight, J.S. Goodling, D.J. Hall, Optimal thermal design of forced convection heat sinks—Analytical, ASME J. Electron. Packaging 113 (1991) 313–321.
[8] J.C.Y. Koh, R. Colony, Heat transfer of microstructures for integrated circuits, Int. Comm. Heat Mass Transfer 13 (1986) 89–98.
[9] S.J. Kim, D. Kim, Forced convection in microstructures for electronic equipment cooling, J. Heat Transfer 121 (1999) 639–645.
[10] S.J. Kim, D. Kim, D.Y. Lee, On the local thermal equilibrium in microchannel heat sinks, Int. J. Heat Mass Transfer 43 (2000) 1735–1748.
[11] T.P. Cotter, Principles and prospects of micro heat pipes, Proc. 5th Int. Heat Pipe Conf., Tsukuba, Japan, pp. 325–328.
[12] A.K. Mallik, G.P. Peterson, M.H. Weichold, Fabrication of vapor-deposited micro heat pipe arrays as an integral part of semiconductor devices, ASME J. Micromech. Syst. 4 (1995) 119–131.
[13] A.K. Mallik, G.P. Peterson, M.H. Weichold, On the use of micro heat pipes as an integral part of semiconductor devices, ASME J. Electron. Packaging 114 (1992) 436–442.
[14] J.P. Holman, Heat Transfer, McGraw-Hill Book Company, New York, 1989.
[15] K. Vafai, C.L. Tien, Boundary and inertia effects on flow and heat transfer in porous media, Int. J. Heat Mass Transfer 24 (1981) 195–203.
[16] C.L. Tien, S.M. Kuo, Analysis of forced convection in microstructures for electronic system cooling, Proc. Int. Symp. Cooling Technology for Electronic Equipment, Honolulu, HI, 1987, pp. 217–226.